COMMUNICATION

Orderly Packed Anodes for High-Power Lithium-Ion Batteries with Super-Long Cycle Life: Rational Design of MnCO$_3$/Large-Area Graphene Composites

Yiren Zhong, Mei Yang, Xianlong Zhou, Yuting Luo, Jinping Wei, and Zhen Zhou*

The burgeoning development of various domains — from portable electronic devices to, especially, electrical vehicles and smart grids — is stimulating the growing appetite for next-generation electrical energy storage (EES) systems with higher power and energy density.[1–3] An effective strategy is to integrate complementary features of uprated EES systems such as supercapacitors into high-performance rechargeable batteries (such as lithium-ion batteries (LIBs)).[4,5] Particularly, since the graphite anodes in commercial LIBs cannot meet such demanding criteria, myriad materials have been explored as promising candidates, such as Si, metal oxides and other conversion-based materials.[6–8] Nevertheless, it remains a crucial challenge to prepare electrode materials that simultaneously offer high capacity, efficient power delivery, and superb stability.[9] To fully realize high power density, orderly packed electrodes have been fabricated by a liquid-mediated method in supercapacitors, leading to superior ion diffusion and compact capacitive energy storage.[10,11] Meanwhile, for LIB electrodes, an alternating layered structure consisting of active materials and graphene is effective in cushioning the large volume changes and upholding the electrode integrity.[4,12,13] Moreover, such a construction with high electrical conductivity improves the utilization of the active materials.[14]

In this scenario, one perfect model for high-power LIBs is to combine an orderly packed structure with an alternating layered configuration into a single unit. With this aim, most previous investigations have concentrated on electrode engineering and always involved specific procedures, such as vacuum filtering, pulsed laser deposition, or dip coating.[15–17] However, so far, the doctor-blade technique still prevails in electrode preparation, owing to its versatility and ease of use, even for industrial fabrication.[18–20] In consequence, in order to facilely attain desirable electrodes on a large scale, it is pivotal to step forward and focus on general materials design with

appropriate structures. Here, we fulfill this purpose by concentrating on intrinsic materials scope and fabricating a novel composite with MnCO$_3$ submicrometer-particles uniformly grafted on large-area graphene (LG, tens of micrometers in length and width). We have demonstrated that LG induces face-to-face self-assembly during ordinary electrode preparation and forms alternating layers with a continuous and close-packed configuration at the electrode level.

Large-area composites were achieved by means of a reactant-conversion route starting from LG and MnOOH precursor. Generally, this delicately designed architecture with self-assembly into orderly packed electrodes offers several advantages as LIB anodes (Figure S1 in the Supporting Information, shows a schematic illustration). First, LG offers perfect large-area support for MnCO$_3$ particles with uniform dispersion, allowing structural re-organization to be accommodated by the space between particles during cycling.[21,22] Second, the continuous graphene networks existing in an ordered macroscopic electrode guarantee outstanding ion diffusion and electronic conduction, readily yielding high power delivery.[11,23] Third, the inter-plane compact configuration of graphene domains provides sustained structural stability and high-packing-density energy storage.[13,24,25] Profiting from the combination of uninterrupted ion transport and effective structural stabilization, the MnCO$_3$-LG electrode delivered excellent electrochemical performance, and represents state-of-the-art design of high-power, high-efficiency, and low-cost anodes for next-generation LIBs.

The LG was prepared by means of chemical exfoliation of natural graphite followed by thermal reduction. For intuitive comparison, graphite flakes with different sizes were utilized to achieve size-controlled fabrication of graphene. As shown in Figure S2 (Supporting Information), LG exhibits a two-dimensional (2D) transparent appearance with typically wrinkled texture, the characteristic size of which is several times that of small-area graphene (SG). We chose MnCO$_3$ as the target not only on account of traditional merits, such as high capacity, eco-friendliness, and abundant resources, but also for cost-effectiveness and low Li-storage plateau.[26,27] The MnCO$_3$-LG composites were synthesized through a facile hydrothermal route, with self-assembly of MnOOH and in situ conversion to MnCO$_3$ on LG nanosheets (Figure S1, Supporting Information). The original 2D structure and large-area features (30–100 μm) of LG were perfectly preserved (as shown by the optical microscopy image in Figure S3 in the Supporting Information), differing from the commonly obtained aerogel consisting of 3D graphene networks. A representative freestanding MnCO$_3$-LG reveals a homogeneous dispersion of particles on expansive

Y. R. Zhong, Dr. M. Yang, X. L. Zhou, Y. T. Luo,
Prof. J. P. Wei, Prof. Z. Zhou
Tianjin Key Laboratory of Metal and Molecule
Based Material Chemistry
Key Laboratory of Advanced Energy Materials Chemistry
(Ministry of Education)
Institute of New Energy Material Chemistry
Collaborative Innovation Center of Chemical Science
and Engineering (Tianjin)
Nankai University
Tianjin 300071, PR China
E-mail: zhouzhen@nankai.edu.cn
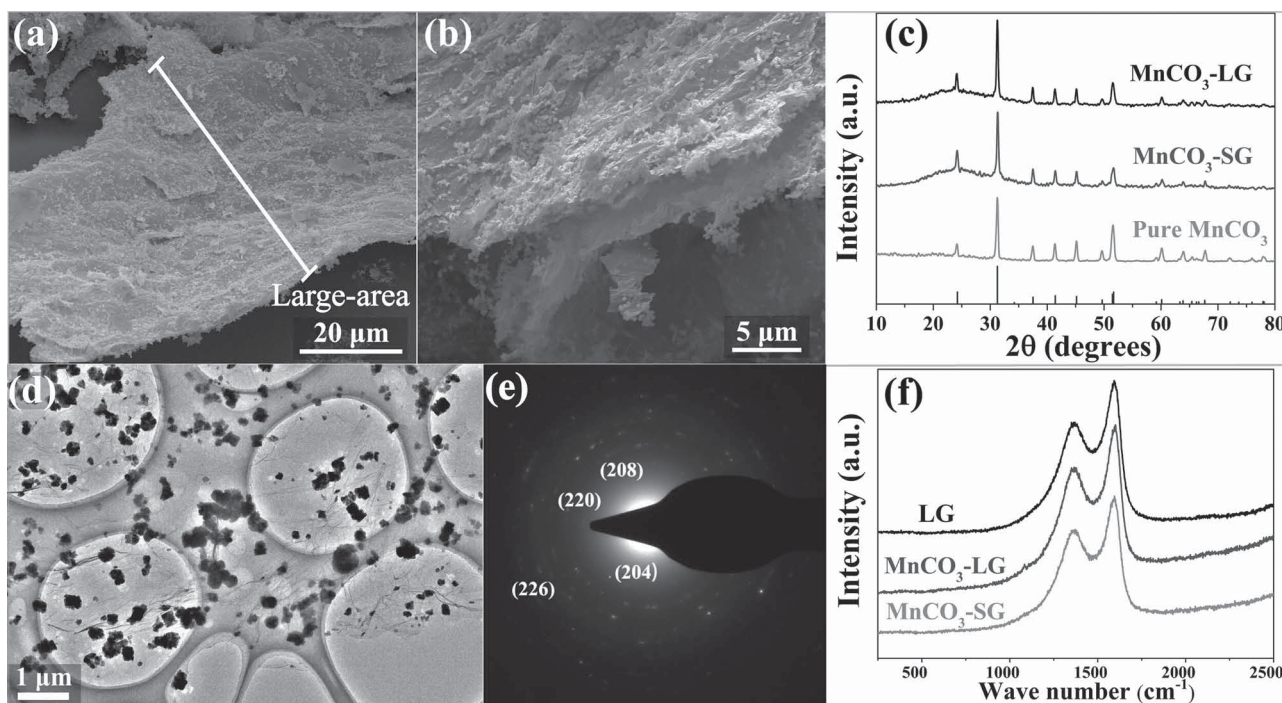
Figure 1. a,b) SEM images of MnCO$_3$-LG under different magnifications. c) XRD patterns of MnCO$_3$–graphene composites and pure MnCO$_3$ samples. d,e) TEM image (d) and SAED pattern (e) of MnCO$_3$-LG. f) Raman spectra of MnCO$_3$–graphene composites and LG.

sheets with overall size up to tens to hundreds of micrometers, which is attributed to the LG assembly (**Figure 1**a). Viewed from the edge (scanning electron microscopy (SEM) image, Figure 1b), the submicrometer-particles sandwiched by graphene are observed as one tectonic unit, forming an alternating architecture as a whole. Transmission electron microscopy (TEM) images also show the uniform distribution of particles (diameters around 300 nm) on transparent sheets, further identifying the ultrathin graphene (Figure 1d), which is also confirmed by dark-field images (Figure S4, Supporting Information). In particular, close observation reveals that the particles exhibit a hierarchical structure composed of many nanorods, which can be traced to in situ conversion of the MnOOH nanorod template (Figure S5, Supporting Information). In contrast, MnCO$_3$-SG materials show the expected small area but similar structure without severe aggregation (Figure S6, Supporting Information).

The X-ray diffraction (XRD) patterns of each sample confirm the pure phase of rhombohedral MnCO$_3$ with a perfect match to each corresponding plane (Figure 1c), which is further affirmed by the selected area electron diffraction (SAED) patterns in Figure 1e. The broad peak at around 25° is attributed to the typical (002) plane of graphene, verifying its existence in the hybrid. Raman spectroscopy is a potent tool for the characterization of carbon materials (Figure 1f). Two obvious peaks at ca. 1369 and ca. 1595 cm^{-1} are observed in the spectra, corresponding to a disorder-induced feature (D-band) and the E_{2g} mode of graphite (G-band).[28] The tiny peak at 1084 cm^{-1} identifies the presence of MnCO$_3$ in the hybrid (Figure S7, Supporting Information). The low D/G band intensity ratio (I_D/I_G) proves the excellent graphitization of graphene with a highly ordered honeycomb lattice. From the slight change of band

ratio in MnCO$_3$-LG (ca. 0.779) compared with LG (ca. 0.761), it is evident that the incorporation of MnCO$_3$ causes slight structural disturbance in graphene. Notably, I_D/I_G for MnCO$_3$-LG is a little lower than for MnCO$_3$-SG (ca. 0.783), which may be related to the large-area character and consequently broader sp^2 domains. To further elucidate the area difference, nitrogen adsorption–desorption measurements were performed, in which the specific surface area (SSA) of MnCO$_3$-LG and MnCO$_3$-SG were calculated as 212.5 and 342.9 m^2 g^{-1}, respectively (Figure S8, Supporting Information). The obvious contrast is attributed to the area characteristics, in particular the edge proportion in graphene, which significantly contributes to the SSA.[29] In brief, LG in hybrid materials processes large graphene domains with relatively low edge proportion, which then generates a lower SSA, further confirming the large-area characteristic. Indeed, owing to their mesoporous structure (average pore diameter of ca. 3 nm), both MnCO$_3$-LG and MnCO$_3$-SG exhibit extremely high SSA compared with the reported hybrid materials, forming open channels favorable for fast ion transport.

This large-scale character endows the composite with unique properties for electrode preparation through the universal doctor-blade method (Figure S1, Supporting Information). The extended and flat graphene nanosheets can self-assemble on the current collector (i.e., Cu foil) with face-to-face packing into an ordered and continuous structure owing to the large interfacial contact area and facile orientation of LG with respect to the Cu foil. These large-area sheets join together and form a smooth, void-free, and interconnected entirety, as shown directly by the front view (**Figure 2**a). The connecting boundaries could be observed clearly for each MnCO$_3$-LG sheet without any pulverization. Moreover, as presented in Figure 2c, the cross-sectional
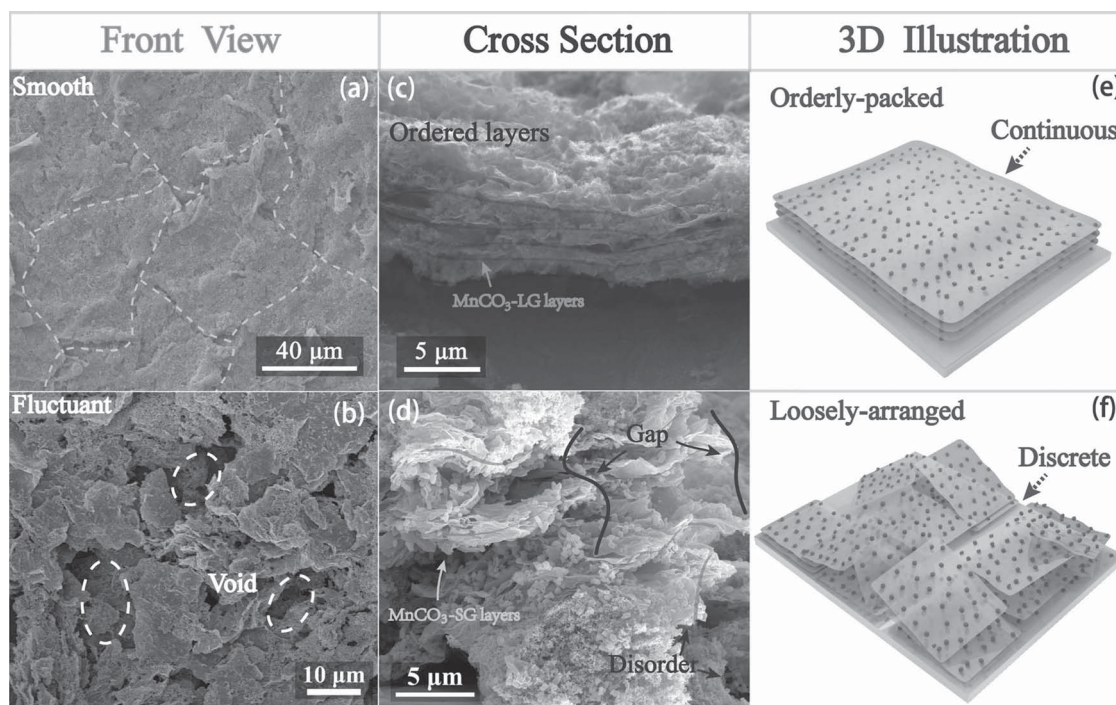
Figure 2. a–d) Morphology characterization including front (a,b) and cross-sectional (c,d) views of the as-prepared electrodes: MnCO$_3$-LG (a,c) and MnCO$_3$-SG (b,d). e,f) 3D illustrations of the corresponding electrodes. The dashed lines in (a) mark the joining boundaries of the composite sheets in the MnCO$_3$-LG electrode surface.

image of the electrode reveals the regular stacking of parallel MnCO$_3$-LG sheets with explicit LG and MnCO$_3$ alternating layers, demonstrating no oblique or vertical alignment within the structure (indicated by translucent gray lines). For the under-sized SG sheets with limited contact surface, such an ordered structure cannot be fully achieved. The MnCO$_3$-SG electrode exhibits an anomalous and discontinuous appearance with the sheets placed tilted with respect to one another and the presence of in-plane voids (Figure 2b). As further explicitly displayed by the cross-sectional image, although some MnCO$_3$-SG layers assume a parallel configuration, obvious in-plane gaps as well as random arrangements between sheets are clearly detected (Figure 2d). As mentioned before, the electrode structure is a significant criterion determining the Li-storage performance. The MnCO$_3$-SG electrode affords only discrete electronic conductivity with long ion diffusion paths, leading to inefficient Li storage, owing to the inter-sheet gaps and disarrangement. In contrast, the electrode based on LG offers fascinating advantages over SG electrodes for energy storage. Because of the ordered and mutually connected configuration, the MnCO$_3$-LG composite creates uninterrupted conductive networks and effective ion transport paths, which result in compact Li storage with high-power performance (**Figures** 2e,f and **3**a).

Galvanostatic measurements were conducted to verify the proposed structural advantages. As demonstrated in Figure S9 (Supporting Information), the MnCO$_3$-LG composite delivered an initial capacity of 880 mAh g^{-1}; this high value is consistent with many results reported for metal carbonate materials.[24,26,30,31] A stable capacity of ca. 1450 mAh g^{-1} is achieved at 200 mAh g^{-1} for 200 cycles, demonstrating huge improvement over pure MnCO$_3$. Note that the composite showed an ever-rising capacity for the whole process. A similar phenomenon was also observed at a high rate of 500 mAh g^{-1}, where the capacity rose from ca. 750 to ca. 1395 mAh g^{-1} in 500 cycles (Figure 3b). This attractive phenomenon is ascribed to the ready re-oxidation of Mn^{II} in MnCO$_3$ to higher valence. For comparison, we also measured MnCO$_3$-SG, which displays a lower capacity of ca. 960 mAh g^{-1}. For comparison, pure graphene delivers only 410 mAh g^{-1}, thus confirming its main function as a conductive matrix. It is known that conversion-based materials (metal oxides, metal oxysalts, etc.) always suffer from poor stability caused by drastic volume change, low conductivity, and thermodynamic irreversibility of discharge products.[32,33] However, all the as-prepared electrodes maintained good cyclic stability for hundreds of cycles at high rates. Hence the robust graphene in our designed structure fully protects the structural integrity.

As for rate performance, although MnCO$_3$-SG displays a comparable capacity at a low current density of 100 mA g^{-1}, the MnCO$_3$-LG electrode shows much better performance and higher capacity retention than MnCO$_3$-SG for ensuing rates (Figure 3c). Stunningly, MnCO$_3$-LG delivers an outstanding capacity of ca. 420 mAh g^{-1} at an intense rate of 10 A g^{-1}, corresponding to an amazing full charge time of 150 s. While the current density reverts to 100 mA g^{-1}, the capacity swiftly recovers its original value of over 1000 mAh g^{-1} and remains steadily ascending. Further, MnCO$_3$-LG electrodes manifest higher Coulombic efficiency than the MnCO$_3$-SG electrodes for the whole rate measurement, which is especially apparent in current-changing cycles (Figure S10, Supporting Information). These results prove that the orderly packed electrodes exhibit better tolerance to fast,
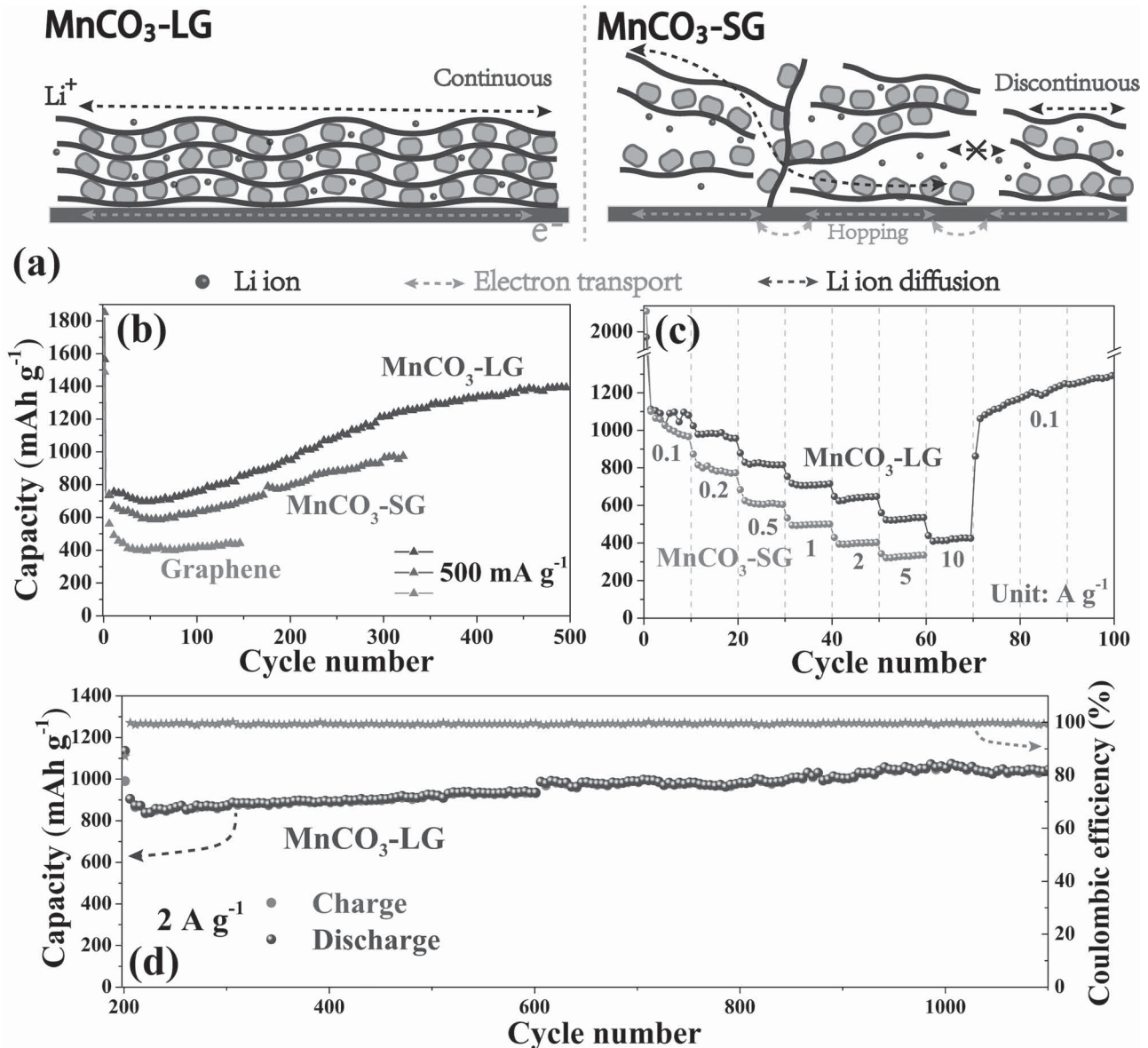
Figure 3. a) Schematic illustrations of electron and ion transport. b,c) Cyclic performances at 0.5 A g^{-1} (b) and rate capabilities (c) of MnCO$_3$-LG and MnCO$_3$-SG. d) Long-term cyclic performance with Coulombic efficiency at 2 A g^{-1} after 200 cycles at 200 mA g^{-1}.

repeated discharge–charge processes, as well as better control of the irreversible capacity than common disordered electrodes.

Given the resemblance of material structures and component contents (details in Figure S11 in the Supporting Information), the capacity difference between these materials should originate from the specific electrode configuration. As reported by Kim et al.,[34] poor connectivity and disorder always induce an increase of carrier-trapping centers (and thus carrier hopping between them), resulting in a decline of carrier mobility according to the thermal carrier trapping and release model.[35] Therefore, the discontinuous network of MnCO$_3$-SG electrodes leads to long ion transportation and especially inferior electrical conductivity at higher rates (such as 500 mA g^{-1}), making part of the MnCO$_3$ particles inaccessible to lithium ions and then unavailable for electrochemical reactions, which is partially confirmed

by electrochemical impedance spectroscopy (EIS) (Figure S12, Supporting Information). As for MnCO$_3$-LG, the continuous network formed by orderly packed LG guarantees an efficient transport path with low electron conduction barriers and short ion diffusion paths, which is vividly summarized in Figure 3a.

To further elucidate the outstanding Li-storage performances, after 200 cycles at 200 mAh g^{-1}, we upgraded the current density to 2 A g^{-1} for long-term cycling (Figure 3d). Under such rapid lithiation/delithiation conditions, MnCO$_3$-LG still manifests an excellent capacity of ca. 1050 mAh g^{-1} after 1100 cycles without capacity loss, signifying simultaneous achievement of superior power delivery and high energy density. The Coulombic efficiency (CE) is a key index for highly reversible Li-storage systems, yet the conversion-based materials are always trapped in ubiquitous large Coulombic inefficiency and round-trip energy loss.[33] Displayed in
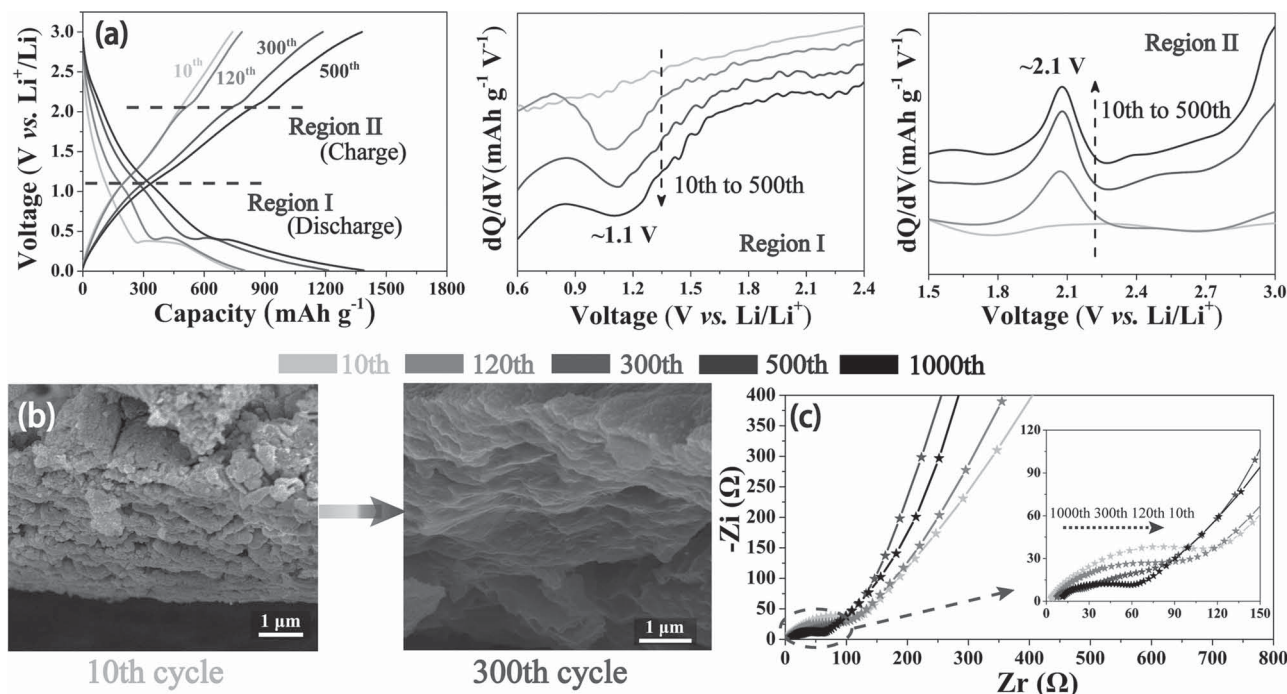
Figure 4. a) Representative discharge–charge curves with corresponding differential charge vs. voltage plots at region I (discharge) and region II (charge), respectively. b) Evolution of the cross section after representative numbers of cycles (10 and 300). c) EIS of typical cycles during the cycling process of the MnCO$_3$-LG electrode.

Figure 3d, right after an adaptation to the current density change in the first cycle, the LG composites show a stable CE of nearly 100%, demonstrating highly efficient Li-storage performance with no detection of structural deterioration or side reactions.

As stated, the MnCO$_3$ composites show a gradually rising capacity even over the course of 500 cycles. We then further explored the electrochemical behaviors of MnCO$_3$-LG electrodes. The cyclic voltammetry (CV) (Figure S13, Supporting Information) curves reveal two corresponding peaks for each scan, indicating the typical redox couple of Mn^{2+}/Mn^0. **Figure 4**a presents the discharge–charge plots of representative cycles, where it is clearly observed that the capacity has nearly doubled after the 500th cycle. To clarify this phenomenon, the plots of differential-capacitance versus voltage were exploited for precise location of redox peaks. In addition to the pair of redox peaks identified in the CV and discharge–charge plots, two new mirror peaks centered at ca. 1.1 and 2.1 V were detected (Figure 4a, regions I and II). It is generally accepted that for many Mn-based materials, the anodic peak at 2.1 V is related to the re-oxidation of Mn^{II} to higher valence.[36,37] The cathodic peak at ca. 1.1 V is ascribed to the corresponding reduction process of a high valence state to Mn^{II}. Note that both peaks emerge after the 50th cycle and their intensities increase over the ensuing cycles, indicating the gradual increase of Mn valence. In view of the fact that the highest valence of stable manganese oxides is Mn^{IV}, the Mn ions in the hybrid may twice undergo an increase in valence, ascending from Mn^{II} to Mn^{IV}, within the whole cycling process, which therefore, accounts for the reasonable elevation of the capacity and was also confirmed by X-ray photoelectron spectroscopy (XPS) (Figure S14, Supporting Information).

In order to better understand the excellent performance of MnCO$_3$-LG, we carried out cycle-dependent characterization of the electrode. Figure S15 (Supporting Information) shows the typical electrode evolution in 1000 cycles. The electrodes maintain an increasingly smooth surface throughout the cycles, with the MnCO$_3$ particles gradually merging into the graphene layer. In particular, a gradually tighter connection between particles is observed with increasing cycle number, which produces improved ion and electron transfer networks and further benefits Li storage under high current densities. As distinctly revealed by cross-section images, both representative electrodes at the 10th and 300th cycles well maintain the original construction with orderly stacked composite layers (Figure 4b). Moreover, compared with the pristine electrode, the cycled electrode shows a more-densely-packed structure, leading to a more efficient character for stable and compact energy storage. Even after 1000 cycles, it is observed that the electrode perfectly maintains the integrity of the layered architecture at all dimensions (Figure S16, Supporting Information). Figure 4c shows EIS results after representative numbers of cycles. It is obvious that the semicircles gradually reduced as the cycling process proceeded. These Nyquist plots consist of the typical characteristic of two corresponding impedances in the media-to-high frequency range, namely the solid electrolyte interface (SEI) resistance (R_{SEI}) and the charge-transfer impedance (R_{ct}). Although the electrolyte resistance increased slightly,[38,39] R_{ct} of the 1000th cycle was significantly decreased compared with initial cycles due to the invariance of R_{SEI}.[13] This huge reduction in R_{ct} signifies the enhanced inter-particle contact and electrical contact between graphene and MnCO$_3$ particles, which is bridged by

continuous graphene networks and also related to the increasingly inter-connected and densely packed structure.

In summary, we have demonstrated an ingenious MnCO₃-LG composite with beneficial effects on efficient preparation of well-organized and compact electrodes. Profiting from the large-area character of expansive graphene nanosheets, the hybrid self-assembled and stacked into an orderly packed, alternating configuration through the ordinary doctor-blade technique without any special treatment. While facilitating an efficient ion-transport path along with uninterrupted electron-conductive networks, such desirable electrodes concurrently achieved high capacity and superior power delivery, representing a power bridge between batteries and supercapacitors. Moreover, accompanied by the favorable promotion of particle connectivity and transport kinetics during cycling, the interlayered graphene effectively released the structural distortion of active materials, ensuring potent protection for ultralong cyclic stability. This large-area graphene hybrid offers a new insight into general materials design towards efficient fabrication of orderly packed electrodes for extended energy storage systems.

Experimental Section

Preparation of LG and SG: Graphite oxide (GO) was prepared from natural graphite flakes by a modified Hummers method. For preparation of graphene, GO was placed in a horizontal tube furnace and thermally treated for 0.5 h at 400 °C in Ar atmosphere with a heating rate of 10 °C min⁻¹. To fabricate large- and small-area graphene, graphite with 80 and 3600 mesh size was utilized as the raw materials, respectively.

Preparation of MnCO₃-LG and MnCO₃-SG composites: MnOOH nanorods were first synthesized as the precursor. Briefly, KMnO₄ (0.316 g) was dissolved in deionized water (35 mL) followed by the slow addition of citric acid (0.19 g). After thorough mixing, the solution was transferred to a poly(tetrafluoroethylene) (Teflon)-lined autoclave and heated at 180 °C for 2 h. For preparation of MnCO₃-graphene composites, graphene (LG or SG, 25 mg) and MnOOH precursor (50 mg) were homo-dispersed in glycol (30 mL) after sonication, and then NaHCO₃ (0.11 g) was slowly added. The above mixture was solvothermally treated at 180 °C for 15 h. Pure MnCO₃ was also prepared by the same procedure without the addition of graphene. The details of materials characterization and electrochemical measurements can be found in the Supporting Information.

Supporting Information

Supporting Information is available from the Wiley Online Library or from the author.

Acknowledgements

[1] J. M. Tarascon, M. Armand, *Nature* **2001**, *414*, 359.

[2] P. G. Bruce, B. Scrosati, J. M. Tarascon, *Angew. Chem. Int. Ed.* **2008**, *47*, 2930.

[3] M. Armand, J. M. Tarascon, *Nature* **2008**, *451*, 652.

[4] X. Zhao, C. M. Hayner, M. C. Kung, H. H. Kung, *Adv. Energy Mater.* **2011**, *1*, 1079.

[5] J. Chmiola, C. Largeot, P. L. Taberna, P. Simon, Y. Gogotsi, *Science* **2010**, *328*, 480.

[6] H. Wu, G. Yu, L. Pan, N. Liu, M. T. McDowell, Z. Bao, Y. Cui, *Nat. Commun.* **2013**, *4*, 1943.

[7] A. Magasinski, P. Dixon, B. Hertzberg, A. Kvit, J. Ayala, G. Yushin, *Nat. Mater.* **2010**, *9*, 353.

[8] M. V. Reddy, G. V. Subba Rao, B. V. Chowdari, *Chem. Rev.* **2013**, *113*, 5364.

[9] J. Goodenough, H. Abruna, M. Buchanan, *Basic Research Needs for Electrical Energy Storage: Report of the Basic Energy Sciences Workshop on Electrical Energy Storage*, US Department of Energy **2007**, DOI: 10.2172/935429.

[10] D. N. Futaba, K. Hata, T. Yamada, T. Hiraoka, Y. Hayamizu, Y. Kakudate, O. Tanaike, H. Hatori, M. Yumura, S. Iijima, *Nat. Mater.* **2006**, *5*, 987.

[11] X. Yang, C. Cheng, Y. Wang, L. Qiu, D. Li, *Science* **2013**, *341*, 534.

[12] J. Chang, X. Huang, G. Zhou, S. Cui, P. B. Hallac, J. Jiang, P. T. Hurley, J. Chen, *Adv. Mater.* **2014**, *26*, 758.

[13] S. J. Prabakar, Y. H. Hwang, E. G. Bae, S. Shim, D. Kim, M. S. Lah, K. S. Sohn, M. Pyo, *Adv. Mater.* **2013**, *25*, 3307.

[14] J. K. Lee, K. B. Smith, C. M. Hayner, H. H. Kung, *Chem. Commun.* **2010**, *46*, 2025.

[15] X. Q. Yu, Y. He, J. P. Sun, K. Tang, H. Li, L. Q. Chen, X. J. Huang, *Electrochem. Commun.* **2009**, *11*, 791.

[16] S. W. Lee, B. S. Kim, S. Chen, Y. Shao-Horn, P. T. Hammond, *J. Am. Chem. Soc.* **2009**, *131*, 671.

[17] C. Ban, Z. Wu, D. T. Gillaspie, L. Chen, Y. Yan, J. L. Blackburn, A. C. Dillon, *Adv. Mater.* **2010**, *22*, E145.

[18] S. W. Lee, B. M. Gallant, H. R. Byon, P. T. Hammond, Y. Shao-Horn, *Energy Environ. Sci.* **2011**, *4*, 1972.

[19] Y. Lu, K. Korf, Y. Kambe, Z. Tu, L. A. Archer, *Angew. Chem. Int. Ed.* **2014**, *53*, 488.

[20] M. H. Ryou, Y. M. Lee, J. K. Park, J. W. Choi, *Adv. Mater.* **2011**, *23*, 3066.

[21] G. Zhou, D.-W. Wang, F. Li, L. Zhang, N. Li, Z.-S. Wu, L. Wen, G. Q. Lu, H.-M. Cheng, *Chem. Mater.* **2010**, *22*, 5306.

[22] Z.-S. Wu, G. Zhou, L.-C. Yin, W. Ren, F. Li, H.-M. Cheng, *Nano Energy* **2012**, *1*, 107.

[23] D. Li, R. B. Kaner, *Science* **2008**, *320*, 1170.

[24] L. Su, Z. Zhou, X. Qin, Q. Tang, D. Wu, P. Shen, *Nano Energy* **2013**, *2*, 276.

[25] S. M. Paek, E. Yoo, I. Honma, *Nano Lett.* **2009**, *9*, 72.

[26] Y. Zhong, L. Su, M. Yang, J. Wei, Z. Zhou, *ACS Appl. Mater. Interfaces* **2013**, *5*, 11212.

[27] S. Devaraj, H. Y. Liu, P. Balaya, *J. Mater. Chem. A* **2014**, *2*, 4276.

[28] Y. Mao, H. Duan, B. Xu, L. Zhang, Y. Hu, C. Zhao, Z. Wang, L. Chen, Y. Yang, *Energy Environ. Sci.* **2012**, *5*, 7950.

[29] L. Zhang, F. Zhang, X. Yang, G. Long, Y. Wu, T. Zhang, K. Leng, Y. Huang, Y. Ma, A. Yu, Y. Chen, *Sci. Rep.* **2013**, *3*, 1408.

[30] a) Z. Ding, B. Yao, J. Feng, J. Zhang, *J. Mater. Chem. A* **2013**, *1*, 11200; b) L. Wang, W. Tang, Y. Jing, L. Su, Z. Zhou, *ACS Appl. Mater. Interfaces* **2014**, *6*, 12346; c) M. A. Garakani, S. Abouali, B. Zhang, C. A. Takagi, Z. L. Xu, J. Q. Huang, J. Huang, J. K. Kim, *ACS Appl. Mater. Interfaces* **2014**, *6*, 18971.

[31] Y. Sharma, N. Sharma, G. V. S. Rao, B. V. R. Chowdari, *J. Mater. Chem.* **2009**, *19*, 5047.

[32] L. Zhang, H. B. Wu, X. W. D. Lou, *Adv. Energy Mater.* **2014**, *4*, 1300958, DOI: 10.1002/aenm.201300958.

[33] J. Cabana, L. Monconduit, D. Larcher, M. R. Palacin, *Adv. Mater.* **2010**, *22*, E170.

[34] Y. Kim, J.-H. Lee, S. Cho, Y. Kwon, I. In, J. Lee, N.-H. You, E. Reichmanis, H. Ko, K.-T. Lee, H.-K. Kwon, D.-H. Ko, H. Yang, B. Park, *ACS Nano* **2014**, *8*, 6701.

[35] S. Baranovski, *Charge Transport in Disordered Solids with Applications in Electronics*, Wiley, Chichester, UK **2006**.

[36] Y. Sun, X. Hu, W. Luo, F. Xia, Y. Huang, *Adv. Funct. Mater.* **2013**, *23*, 2436.

[37] H. Jiang, Y. Hu, S. Guo, C. Yan, P. S. Lee, C. Li, *ACS Nano* **2014**, *8*, 6038.

[38] F. Wu, J. T. Lee, A. Magasinski, H. Kim, G. Yushin, *Part. Part. Syst. Charact.* **2014**, *31*, 639.

[39] X. Wang, Q. Weng, X. Liu, X. Wang, D. M. Tang, W. Tian, C. Zhang, W. Yi, D. Liu, Y. Bando, D. Golberg, *Nano Lett.* **2014**, *14*, 1164.